AGU PUBLICATIONS

Paleoceanography

RESEARCH ARTICLE
10.1002/2016PA002957

Key Points:
- EEA middepth water temperatures were elevated by 3.9 and 5.2°C during Heinrich event 1 and Younger Dryas, respectively
- Our study documents a large-scale and basin-wide warming across the thermocline and middepth of the tropical Atlantic during H1 and YD
- Our study reveals a lack of a distinctive signature of radiocarbon depletion in EEA middepth during H1 and YD

Correspondence to:
S. Weldeab,
weldeab@geol.ucsb.edu

Citation:
Weldeab, S., T. Friedrich, A. Timmermann, and R. R. Schneider (2016), Strong middepth warming and weak radiocarbon imprints in the equatorial Atlantic during Heinrich 1 and Younger Dryas, *Paleoceanography*, *31*, 1070–1082, doi:10.1002/2016PA002957.

Received 30 MAR 2016
Accepted 2 JUL 2016
Accepted article online 11 JUL 2016
Published online 14 AUG 2016

Strong middepth warming and weak radiocarbon imprints in the equatorial Atlantic during Heinrich 1 and Younger Dryas

Syee Weldeab[1], Tobias Friedrich[2], Axel Timmermann[2], and Ralph R. Schneider[3]

[1]Department of Earth Science, University of California, Santa Barbara, California, USA, [2]International Pacific Research Center, School of Ocean and Earth Science and Technology, University of Hawaii at Manoa, Honolulu, Hawaii, USA, [3]Institute of Geosciences, Kiel University, Kiel, Germany

Abstract We present a benthic foraminiferal multiproxy record of eastern equatorial Atlantic (EEA) middepth water (1295 m) covering the last deglacial. We show that EEA middepth water temperatures were elevated by 3.9 ± 0.5°C and 5.2 ± 1.2°C during Heinrich event 1 (H1) and Younger Dryas (YD), respectively. The radiocarbon content of the EEA middepth during H1 and YD is relatively low and comparable to the values of the pre-H1 episode and Bølling-Allerød, respectively. A transient Earth system model simulation, which mimics the observed deglacial Atlantic Meridional Overturning Circulation (AMOC) history, qualitatively reproduces the major features of the EEA proxy records. The simulation results suggest that fresh water-induced weakening of the AMOC leads to a vertical shift of the horizon of Southern Ocean-sourced water and a stronger influence of EEA sea surface temperatures via mixing. Our findings reaffirm the lack of a distinctive signature of radiocarbon depletion and therefore do not support the notion of interhemispheric exchanges of strongly radiocarbon-depleted middepth water across the tropical Atlantic during H1 and YD. Our temperature reconstruction presents a critical zonal and water depth extension of existing tropical Atlantic data and documents a large-scale and basin-wide warming across the thermocline and middepth of the tropical Atlantic during H1 and YD. Significant difference in the timing and pace of H1 middepth warming between tropical Atlantic and North Atlantic likely points to a limited role of the tropical Atlantic middepth warming in the rapid heat buildup in the North Atlantic middepth.

1. Introduction

The deglacial climate transition from the Last Glacial Maximum to the Holocene was interrupted by two major returns to cold conditions associated with the Heinrich 1 (H1) and Younger Dryas (YD) events [*Hemming*, 2004; *Liu et al*., 2009; *Marcott et al*., 2014; *NGRIP-members*, 2004; *Shakun et al*., 2012]. Though some studies suggest that ice sheet instabilities are not the trigger of the onset of H1 and YD [*Alvarez-Solas et al*., 2013; *Barker et al*., 2015; *Thornalley et al*., 2010], ice sheet instabilities and meltwater-induced weakening of the Atlantic Meridional Overturning Circulation (AMOC) are considered by others as one of the major forcings of the climate perturbations during H1 and YD [*Liu et al*., 2009; *McManus et al*., 2004; *Menviel et al*., 2011; *Renssen et al*., 2015; *Timmermann et al*., 2005]. Subsurface warming in and northward heat transport from the tropical Atlantic may have contributed to North Atlantic middepth warming which has been invoked as a terminating process for the H1 and YD events [*Dokken et al*., 2013; *Marcott et al*., 2011; *Petersen et al*., 2013; *Shaffer*, 2004; *Thiagarajan et al*., 2014]. The magnitude and spatial extent of tropical Atlantic middepth warming and its temporal and causal relationship to the middepth warming in the North Atlantic is, however, not well established. Most of the middepth oceanographic reconstructions in the tropical Atlantic are limited to the western part of the basin and quantitative reconstruction of middepth temperature is very limited [*Came et al*., 2007, 2008; *Freeman et al*., 2015; *Huang et al*., 2014; *Lund et al*., 2015; *Lynch-Stieglitz et al*., 2014; *Mangini et al*., 2010; *Oppo et al*., 2015; *Rühlemann et al*., 2004; *Schmidt et al*., 2012; *Sortor and Lund*, 2011; *Xie et al*., 2012, 2014]. Here we focus on the middepth of the eastern equatorial Atlantic (EEA) and examine last deglacial oceanographic changes using sensitive Mg/Ca paleothermometry and benthic foraminiferal Ba/Ca, $\delta^{13}C$, and $\Delta^{14}C$ reconstructions. Our proxy records along with the results of a transient model simulation reveal a substantial difference in the temporal evolution of middepth warming in the tropical and North Atlantic consistent with the idea of a limited thermal exchange between the tropical and North Atlantic during H1.

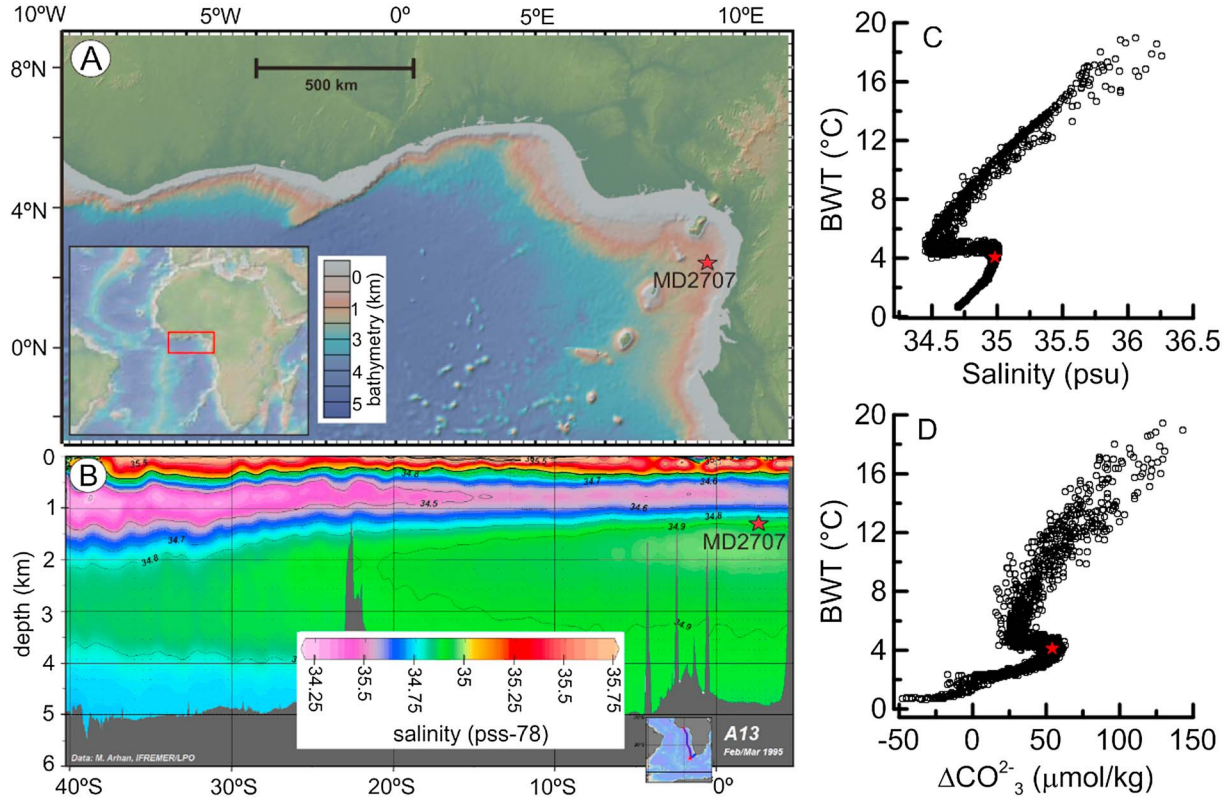

Figure 1. (a) Bathymetric map of the eastern equatorial Atlantic created using GeoMapApp software [*Ryan et al.*, 2009] and (b) salinity profile across a meridional transect (profile A13 of WOCE) [*Schlitzer*, 2000]. (c, d) Temperature-salinity and temperature-ΔCO_3^{2-} relationships in the Gulf of Guinea (latitude: 10.84 N–5.72 S and longitude: 338.77°E–306.35°E, water depth: 0–5800 m). Red star indicates the location and environmental parameters at MD03-2707 core site. All data sets shown in Figures 1c and 1d were retrieved from the Global Ocean Data Analysis Project (GLODAP) [*Key et al.*, 2004]. Carbonate ion concentrations ΔCO_3^{2-} were calculated using the CO_2-CALC software [*Robbins et al.*, 2010].

2. Setting and Methods

2.1. Setting and Proxy Data

We focus on the MD03-2707 marine core sediment that was recovered from the eastern equatorial Atlantic (02°30.11′N, 09°23.68′E, water depth 1295 m) (Figure 1a). Water column profiles of salinity, salinity-temperature, and temperature-ΔCO_3^{2-} (= in situ CO_3^{2-} minus saturation CO_3^{2-}) relationships show that the core site is currently located in the transition zone between North Atlantic Deep Water (NADW) and Antarctic Intermediate Water horizon (AAIW) (Figure 1). At the location of MD03-2707 the bottom water is characterized by salinity, temperature, and ΔCO_3^{2-} of 34.8 practical salinity unit (psu), 4.2°C, and 50 μmol/kg, respectively (Figures 1b–1d).

MD03-2707 consists of a 37.4 m long core sediment that continuously covers the last 155 thousand years before present (kyr B.P.) [*Weldeab et al.*, 2007]. In this study, we focus on the sediment depth between 497.5 and 802 cm that covers the time window between 10 and 20.5 kyr B.P. (Figure 2). Radiocarbon measurements in tests of benthic and planktonic foraminifers (see below) were carried out at the Leibniz Labor for Radiometric Dating, University of Kiel, Germany.

We added seven (7) new radiocarbon datings of *Globigerinoides ruber* (pink) tests to the existing nine (9) radiocarbon data of the same species in the target sediment section [*Weldeab et al.*, 2007]. The age model and age model uncertainty of the target sediment segment are established using 23 radiocarbon datings of *Globigerinoides ruber* pink, the Marine13 data set [*Reimer et al.*, 2013], a constant reservoir age correction of 400 years, and the Bayesian statistical software "Bacon" [*Blaauw and Christen*, 2011] (Figure 2).

We carried out 13 radiocarbon datings of mixed epibenthic foraminifers (*Cibicides* spp.). We calculated the $\Delta^{14}C$ (‰) of bottom water using the equation formulated by *Adkins and Boyle* [1997]: $\Delta^{14}C$ (‰) = $[(e^{-14C\ age/8033})/(e^{-cal\ age/8266}) - 1] \times 1000$, with cal age and ^{14}C being calendar age of the sediment (Figure 2) and radiocarbon

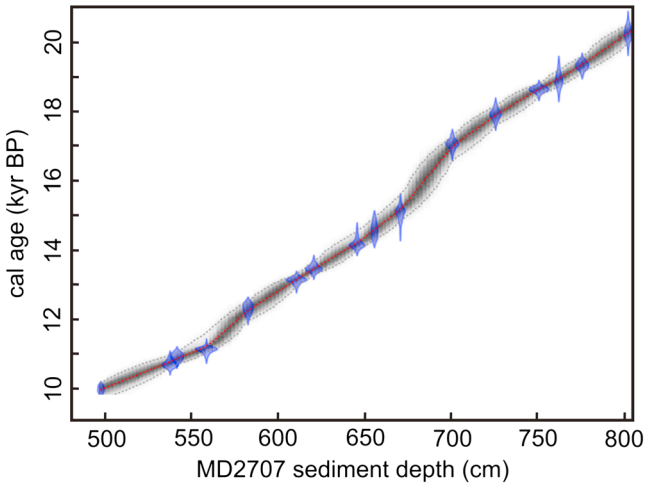

Figure 2. Age model of MD03-2707 target segment (497.5–802 cm) based on 16 radiocarbon data of *G. ruber* pink tests, constant reservoir age correction of 400 years and calculated using Bacon, a Bayesian statistics software [*Blaauw and Christen*, 2011]. Calibrate age model control points (blue) and the age-depth model with gray stippled lines showing 95% confidence intervals and red curve showing a single "best" model based on the weighted mean age for each depth.

age of benthic foraminifers, respectively. Analysis of $\delta^{18}O$ and $\delta^{13}C$ in *Cibicides pachyderma* from MD03-2707 down core samples was made with Thermo MAT 253 mass spectrometer coupled online to the Kiel Carbonate Device Type IV for automated CO_2 preparation. Analytical uncertainty is 0.07‰ and 0.03‰ for $\delta^{18}O$ and $\delta^{13}C$, respectively. We carried out trace element analyses in tests of *Cibicides pachyderma* and in combined tests of *Globobulimina affinis* and *Globobulimina* cf. *pacifica* that were selected from a sample fraction of 250–400 μm. We combined the infaunal species *Globobulimina affinis* and *Globobulimina* cf. *pacifica* because the abundance of one of these species was not high enough for a robust trace element analysis. The cleaning of gently crushed foraminiferal test includes oxidative and reductive steps [*Martin and Lea*, 2002, and reference therein]. Trace elements were analyzed by the isotope dilution/internal standard method [*Martin and Lea*, 2002] using a Thermo Finnigan Element2 sector inductively coupled plasma mass spectrometer (ICP-MS). Analytical reproducibility, assessed by analyzing consistency standards matched in Mg/Ca and Ba/Ca ratios to dissolved foraminifera solutions, is estimated at ±0.9% (±0.03 mmol/mol) and ±2.4% (±0.065 μmol/mol), respectively. Because of its relatively high sensitivity to calcification temperature [*Skinner and Elderfield*, 2007; *Weldeab et al*., 2016] we use Mg/Ca in *Globobulimina* spp. for bottom water temperature (BWT) reconstruction. We converted the Mg/Ca time series into BWT estimates using Mg/Ca-temperature calibration equation (Mg/Ca[mmol/mol] = (0.36 ± 0.02)*BWT[°C] + 2.22 ± 0.19, $r^2 = 0.92$) that was developed based on Mg/Ca analysis in *Globobulimina* spp. (*Globobulimina affinis* and *Globobulimina* cf *pacifica*) of 39 Gulf of Guinea core top samples [*Weldeab et al*., 2016].

2.2. Model Simulation

We use the three-dimensional atmosphere-vegetation-ocean sea ice-carbon cycle model LOVECLIM [*Goosse et al*., 2010]. The ocean-sea ice component of LOVECLIM (CLIO) consists of a primitive equation ocean general circulation model with a resolution of 3 × 3 [*Goosse et al*., 1999]. CLIO uses a free surface and is coupled to a dynamic-thermodynamic sea ice model [*Fichefet et al*., 1994; *Fichefet and Maqueda*, 1997]. There are 20 unevenly spaced levels in the vertical with thicknesses ranging from 10 m near the surface to ~700 m below 3000 m. The strength of vertical mixing is coupled to the roughness of bottom topography [*Decloedt and Luther*, 2010] as presented in *Friedrich et al*. [2011]. Mixing along isopycnals, the effect of mesoscale eddies on transports and mixing as well as downsloping currents over continental shelves is parameterized [*Goosse et al*., 2010]. The atmospheric component of LOVECLIM is the ECBilt model, a spectral T21 model based on quasi-geostrophic equations extended by estimates of ageostrophic forcing terms [*Opsteegh et al*., 1998]. It consists of three levels in the vertical and contains a full hydrological cycle that is closed over land by a bucket model for soil moisture and a runoff scheme. The atmosphere, ocean, and sea ice components of the LOVECLIM model are coupled by exchange of momentum, heat, and freshwater. The marine carbon cycle component of LOVECLIM is the Liège Ocean Carbon Heteronomous (LOCH) model [*Mouchet*, 2011]. LOCH is a three-dimensional ocean carbon cycle model with prognostic equations for dissolved inorganic carbon, total alkalinity, phosphate, dissolved and particulate organic matter, silicate, and radiocarbon. LOCH is coupled to CLIO using the same time step. Biogeochemical tracers that are subject to advection and mixing are advected and mixed using the same circulation fields and mixing parameters, respectively, as in CLIO. The surface partial pressure of CO_2 is computed from total alkalinity, dissolved inorganic carbon,

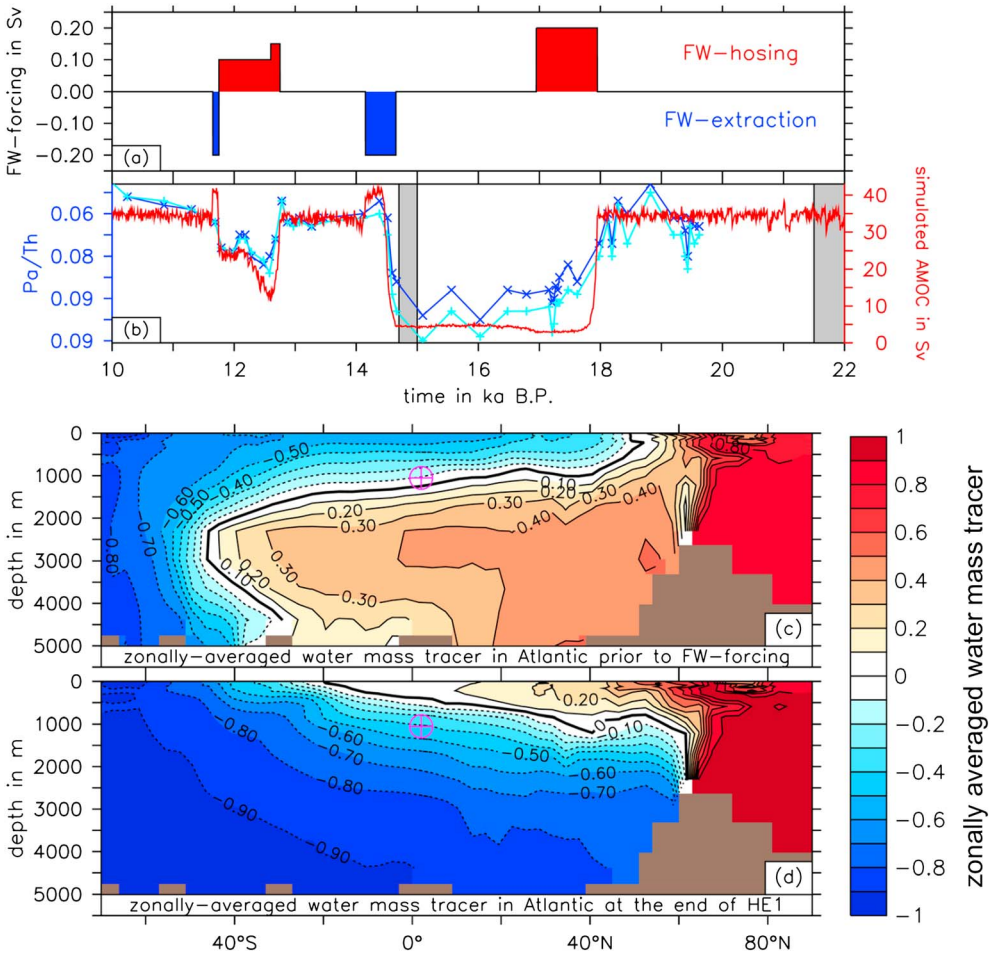

Figure 3. (a) Freshwater (FW) forcing used in the transient model simulation in Sv (1 Sv = 10^6 m^3/s). Positive (negative) values indicate hosing (extraction). FW forcing is applied over the North Atlantic approximately between 50°N–70°N. (b) Simulated strength of the AMOC in Sv (red) compared to $^{231}Pa/^{230}Th$ data (blue, cyan) [*McManus et al.*, 2004]. Gray vertical bars indicate averaging intervals for Figures 3c and 3d, respectively. (c) Water mass tracer zonally averaged over Atlantic prior to FW forcing. See right gray vertical bar in Figure 3b for averaging interval. (d) Water mass tracer zonally averaged over Atlantic at the end of simulated H1. See left gray vertical bar in Figure 3b for averaging interval. Magenta cross in Figures 3c and 3d indicates location of core MD03-2707.

temperature, and salinity. The parameterization of CO_2 exchange with the atmosphere follows *Wanninkhof* [1992]. More details on the LOVECLIM model can be found in *Goosse et al.* [2010].

Experimental Design: The LOVECLIM model is used to perform a transient simulation covering the period of 22–10 ka B.P. The transient simulation is forced by the time evolution values of atmospheric CO_2 concentrations [*Luthi et al.*, 2008]. Orbital parameters vary set according to *Berger* [1978] and Northern Hemispheric ice sheet extent and height are obtained from a recent ice sheet simulation [*Ganopolski and Calov*, 2011]. Orbital parameters and greenhouse gas concentrations are updated every model year. Ice sheet extent and height are updated every 100 model years. In order to avoid internally generated, self-sustained oscillations of the AMOC [*Friedrich et al.*, 2010], a constant Last Glacial Maximum (LGM) bathymetry [*Roche et al.*, 2007] is used. The model is spun up for 10,000 model years using constant climate boundary conditions of 22 kyr B.P. to account for the long equilibration timescale of marine radiocarbon. Atmospheric radiocarbon is not transient but set to 0‰ throughout the entire simulation. The rationale behind this simplified approach is the focus on the effects of ocean circulation changes on marine radiocarbon. The latter become better identifiable when large changes in atmospheric radiocarbon [*Reimer et al.*, 2013] are omitted in the simulation.

Freshwater (FW) forcing is applied to the North Atlantic region ~50°N–70°N to mimic AMOC changes during the H1-Bølling-Allerød (BA)-YD transition (Figures 3a and 3b). The FW forcing is applied without the use of salt

compensation as the latter leads to artifacts in the response of the ocean circulation [*Stocker et al*., 2007]. For Heinrich Event 1, a substantial weakening of the AMOC around 18 kyr B.P. is generated by FW hosing over the North Atlantic with a strength of 0.2 sverdrup (Sv) (1 Sv = 10^6 m^3/s) and a duration of 1000 model years (Figure 3a). After ~3300 model years a pulse of 0.2 Sv FW extraction is applied for 500 model years resulting in the recovery of the AMOC (Figure 3b). The YD period is simulated by slightly weaker and shorter FW forcing. It should be noted that the FW forcing is idealized, and it is not intended to represent recorded changes in sea level or ice-rafted debris. Strength and duration of the forcing has been chosen according to the model's AMOC sensitivity as well as to simulate a temporal evolution of the AMOC that is in qualitative agreement with the Bermuda Rise $^{231}Pa/^{230}Th$ record [*McManus et al*., 2004] (Figure 3b). The latter is largely corroborated by a spatially comprehensive study [*Bradtmiller et al*., 2014], although the spatial pattern is complex, indicating that $^{231}Pa/^{230}Th$ may harbor imprints other than that of deglacial AMOC changes. An additional passive tracer was added to the ocean model to elucidate the response of the Atlantic water mass composition to the large-scale ocean circulation changes generated in the wake of the recurring AMOC weakening-recovery cycle during the H1-BA-YD transition. The tracer is designed to distinguish between southern sourced and northern sourced water masses. To represent a Southern Hemisphere end-member, the passive tracer is restored to a value of −1 at the surface of the Southern Ocean south of 60°S using a relaxation timescale of 10 days. For the North Atlantic the tracer is designed to represent NADW and is restored to a value of +1 at the surface of the North Atlantic between ~55°N and 70°N. Outside the restoring areas the tracer can evolve freely and is advected and mixed as all other tracers of the ocean model. The specific design of the water mass tracer allows identifying a local water mass composition by comparing the local value to the end-member values of ±1.

The zonal mean of the water mass tracer for the Atlantic after the model spin-up is shown in Figure 3c. The two end-member regions can be clearly discerned. The southward propagation of NADW can be identified by a tongue of high values at depths of around 2500 m. Due to northward transport of near-surface waters from the Southern Hemisphere to the North Atlantic, the surface is characterized by lower values and thus a stronger impact of Southern Hemisphere waters. Below the main depth of NADW, the increasing impact of Antarctic Bottom Water (AABW) can be seen from lower values of the water mass tracer. Overall it must be noted, however, that the tracer can only identify the respective fraction of one water mass with respect to its antagonistic water mass based on their geographical origin. Despite this caveat, the water mass tracers will be important assets for our analysis of the change in tropical Atlantic water mass composition during the last glacial termination.

3. Results and Discussion

The temporal focus of this study is centered on the time interval between 9.5 and 20.5 kyr B.P. (Figure 2) and aims to shed light on the oceanographic conditions of the EEA during the last deglaciation. The sediment accumulation in the investigated MD2707 section varies between 16 and 50 cm/kyr (Figure 2). With a sampling interval of 2 cm, the resolution of the proxy time series varies between centennial and multidecadal. Between 20.5 ± 0.4 and 18 ± 0.4 kyr B.P. the $\delta^{18}O$, Ba/Ca, and Mg/Ca time series show little variance with average values of 4.12 ± 0.16‰, 1.88 ± 0.35 μmol/mol, and 3.5 ± 0.22 mmol/mol (3.9 ± 0.6°C), respectively (Figure 4). The $\delta^{13}C$ exhibits an average value of 0.38 ± 0.13‰ with large fluctuations (19–20.5) that do not show a clear trend. Over the same time window, the $\Delta^{14}C$ of bottom water varies between 262 ± 27 and 169 ± 27‰, respectively (Figure 4e). Starting at 17.5 ± 0.4 kyr B.P., Ba/Ca and Mg/Ca rise and $\delta^{18}O$ and $\delta^{13}C$ decline synchronously, reaching plateau values between 16.6 ± 0.5 and 14.0 ± 0.2 kyr B.P. (Figure 4). Concomitant with these changes, benthic foraminiferal $\Delta^{14}C$ drops from 247 ± 32‰ to 46 ± 6‰. Between 14.5 ± 0.2 and 13 kyr B.P. Ba/Ca and Mg/Ca drop significantly and $\delta^{13}C$ increases, on average, by 0.3‰. Starting at 12.9 ± 0.17 kyr B.P. Mg/Ca and $\delta^{18}O$ continue to rise and peak at 12 ± 0.34 kyr B.P. These changes are, however, not accompanied by significant and systematic changes in $\delta^{13}C$ and $\Delta^{14}C$. A brief and significant Ba/Ca decline is centered at 12.3 ± 0.1 kyr B.P. Starting at 11.6 ± 0.36 kyr B.P., Mg/Ca declines rapidly and reaches at 9.6 kyr B.P. a value of 3.07 mmol/mol (Figure 4d). We removed the temperature effect from benthic foraminiferal $\delta^{18}O$ and obtained an estimate $\delta^{18}O$ of seawater that is a composite local salinity and global level changes. The low resolution and relatively large error allow only insights into an orbital-scale trend that, as expected, appear to be dominated by the size of the ice sheets. We note that the Mg/Ca series was presented in *Weldeab et al*. [2016] without discussing the temporal and paleoclimatic context of the record.

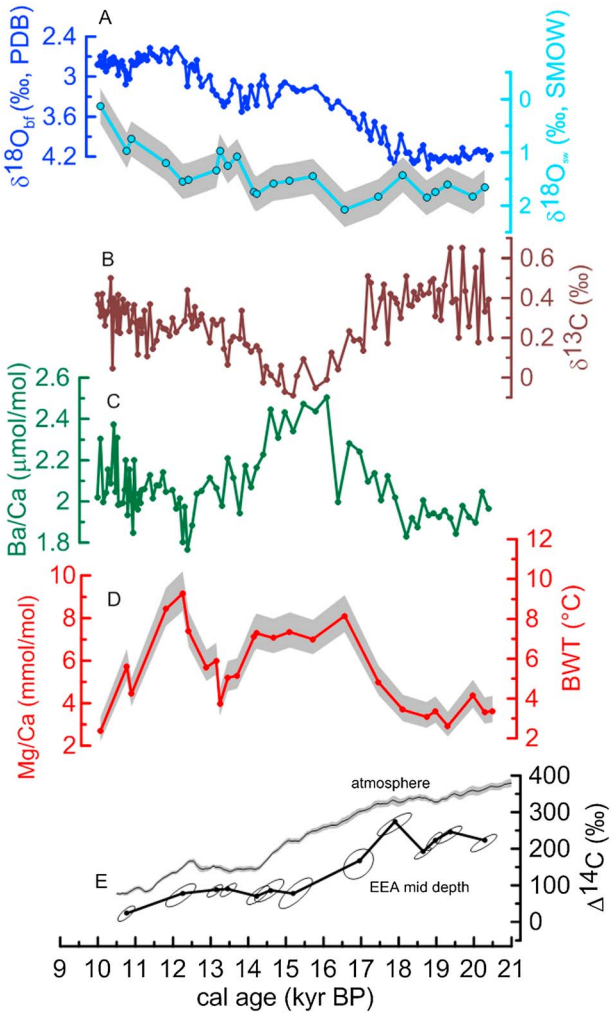

Figure 4. Benthic foraminiferal time series analyzed in samples from MD03-2707 core sediment. (a–c) Stable isotopes and Ba/Ca analyzed in *Cibicides pachyderma* and estimates of $\delta^{18}O$ and its uncertainty (gray envelop). (d) Mg/Ca and Mg/Ca-based bottom water temperature (BWT) estimates. The gray envelop indicates the uncertainty of the BWT estimate. (e) $\Delta^{14}C$ of the atmosphere [*Reimer et al.*, 2013] and EEA bottom water calculated using ^{14}C ages. Gray envelop and ellipses indicate $\Delta^{14}C$ uncertainty that arises due to analytical and age model uncertainties.

3.1. Middepth Warming and Water Mass Changes

The most prominent features of our multiproxy record are centered between 17.5 ± 0.3 and 14.5 ± 0.2 kyr B.P. and between 12.9 ± 0.2 and 11.6 ± 0.2 kyr B.P. (Figures 4 and 5). Taking into consideration age model uncertainties, these two episodes are synchronous with the timing of H1 and YD. During H1, $\delta^{13}C$ and Ba/Ca in *Cibicides pachyderma*, an epibenthic foraminifera, show a negative and positive trends, respectively (Figures 4d and 4e). $\delta^{13}C$ in benthic foraminifers is used as a proxy for the $\delta^{13}C$ signature of dissolved inorganic carbon (DIC) that, in turn, is used as a qualitative indicator for source and age of the water mass [*Oppo et al.*, 2015, and reference therein]. Ba/Ca in benthic foraminifers is used as a proxy for refractory nutrients [*Hall and Chan*, 2004; *Lea and Boyle*, 1989]. Several processes can, however, complicate the interpretation of these proxies. The lowest benthic foraminiferal $\delta^{13}C$ value (0.01 ± 0.06‰) is centered between 16.5 and 14.5 kyr B.P. and falls within the timing of a rapid drop of $\delta^{13}C$ of atmospheric CO_2 ($\delta^{13}C_{atmosphere}$) from −6.5 ± 0.05‰ to −6.8 ± 0.05‰ [*Schmitt et al.*, 2012]. Estimates of past air-sea gas exchange rates are highly uncertain [*Gebbie*, 2014; *Schmittner et al.*, 2013]. However, as shown in a model simulation [*Menviel et al.*, 2012], without invoking changes in ocean circulation or export productivity a temperature-corrected $\delta^{13}C_{atmosphere}$ drop of 0.3 ± 0.01‰ can explain only a negligible fraction of a 0.3‰ decrease in the EEA $\delta^{13}C$ record. The $\delta^{13}C$ record of *G. ruber* pink (a mixed layer dweller) in MD03-2707 shows relatively low values (mean value: 1.23 ± 0.1‰, $n = 21$) during H1 relative to the pre-H1 episode (mean value: 1.49 ± 0.13‰, $n = 61$) (Figure 5). Whereas low $\delta^{13}C$ value of upwelled DIC is reflected by low $\delta^{13}C$ values in *G. ruber* tests, low CO_3^{2-} concentration and low temperature, which characterize upwelled waters, have the opposite effect (i.e., high $\delta^{13}C$) and a significantly stronger impact on $\delta^{13}C$ of *G. ruber* tests [*Peeters et al.*, 2002]. The relatively low $\delta^{13}C$ of *G. ruber* pink and continuous sea surface temperature (SST) increase (Figures 5j and 5k) during H1, therefore, argue against wind-induced upwelling. Similarly, low Ba/Ca values in *G. ruber* pink (Figure 5l), a proxy for runoff [*Weldeab et al.*, 2007, 2014a, 2014b], do not support enhanced runoff and an elevated riverine nutrient supply to the surface water. We conclude, therefore, that proxies for sea surface conditions indicate a relatively low surface productivity and, by inference, most likely reduced export productivity. Furthermore, the increase of benthic foraminiferal Ba/Ca and its decoupling from the magnitude and trend of Ba/Ca in *G. ruber* (Figures 5e and 5l) supports our argument that the bottom water enrichment in refractory nutrients is unrelated to changes in surface water processes. We thus infer that the

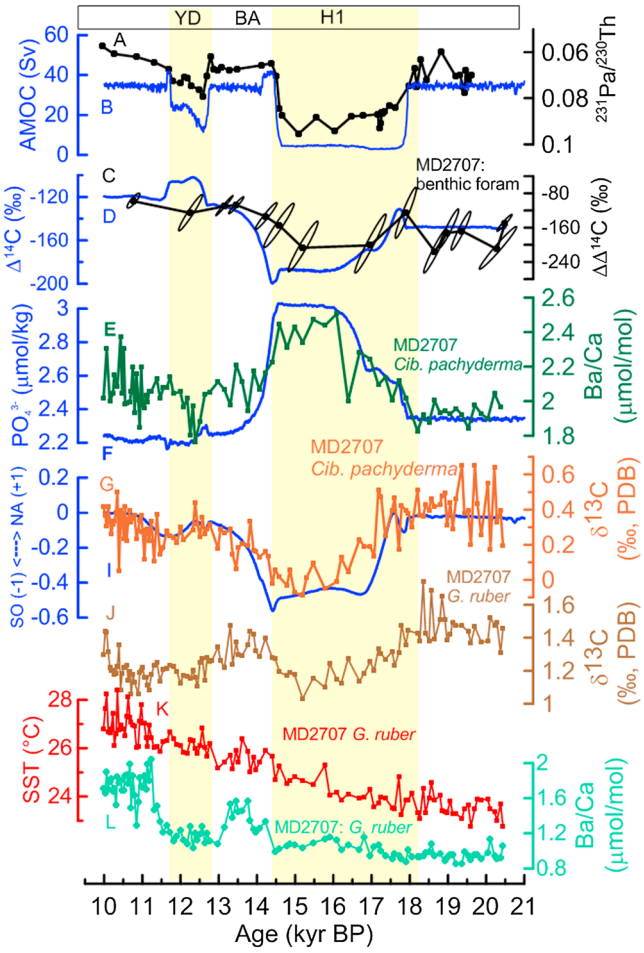

Figure 5. Results of proxy and model simulation analyses. (a) $^{231}Pa/^{230Th}$ time series [*McManus et al.*, 2004], a proxy for changes in AMOC strength, (b) simulated AMOC response to freshwater forcing, (c) $\Delta\Delta^{14}C$ ($\Delta^{14}C_{benthic\ foraminifer} - \Delta^{14}C_{atmosphere}$), (d) $\Delta^{14}C$: simulated changes in ^{14}C at the water depth of MD2707 site relative to the ^{14}C values at the start of the experiment, (e) Ba/Ca in tests of *Cibicides pachyderma*, (f) simulated changes in phosphate concentration, (g) $\delta^{13}C$ analyzed in tests of *Cibicides pachyderma*, and (i) simulated changes in water mass influence of the Southern Ocean (−1) and North Atlantic (+1) end-members at MD2707 site. (j) $\delta^{13}C$ of *G. ruber* pink, (k) Mg/Ca-based SST estimates [*Weldeab et al.*, 2007], and (l) Ba/Ca in *G. ruber* pink, a proxy for a relative runoff estimates [*Weldeab et al.*, 2007].

increase and decrease of the benthic foraminiferal Ba/Ca and $\delta^{13}C$, respectively, reflect changes in residence time or source of the bottom water. An increase of ventilation age or an inflow of radiocarbon-depleted water during the H1 episode is indicated by slightly reduced $\Delta\Delta^{14}C$ values ($\Delta\Delta^{14}C = \Delta^{14}C_{water} - \Delta^{14}C_{atmosphere}$) relative to the values of the Bølling-Allerød (Figure 5c). We note, however, that prior to H1 the $\Delta\Delta^{14}C$ record already shows relatively low values that considering the uncertainty in $\Delta\Delta^{14}C$ estimates are essentially indistinguishable from those of the H1 episode. Therefore, in contrast to the enrichment of refractory nutrients (Figures 5e and 5g) and consistent with the coral-based $\Delta\Delta^{14}C$ record from the EEA [*Chen et al.*, 2015], our $\Delta\Delta^{14}C$ record does not reveal a distinctive feature that is exclusively and unambiguously associated with the H1 episode.

The Mg/Ca-based BWT reconstruction reveals episodes of significant bottom warming (Figure 4d). It is also known that changes in carbonate ion concentration, expressed as ΔCO_3^{2-}, affect benthic foraminiferal Mg/Ca [*Elderfield et al.*, 2006; *Marchitto et al.*, 2007a; *Rosenthal et al.*, 2006; *Weldeab et al.*, 2016]. Sensitivity of Mg/Ca in *Globobulimina* spp. to changes in $\Delta CO_{3\ pore\ water}^{2-}$ is estimated to be 0.009 ± 0.0044 mmol/mol per unit ΔCO_3^{2-} (μmol/kg) [*Weldeab et al.*, 2016]. While, to our knowledge, there is no ΔCO_3^{2-} reconstruction available for the water depth of our core location, a low resolution record from the EEA (water depth: 2945 m) indicates a $\Delta CO_{3\ bottom\ water}^{2-}$ change of 9 μmol/kg from the last glacial (36.4 ± 7.4 μmol/kg) to the early Holocene (27.1 ± 6.4 μmol/kg). According to *Weldeab et al.* [2016], the $\Delta CO_{3\ bottom\ water}^{2-}$ change of 9 μmol/kg would correspond to a $\Delta CO_{3\ pore\ water}^{2-}$ change of 22 μmol/kg and a potential bias of 0.6 ± 0.3°C in the BWT estimate, which is within the uncertainty of the Mg/Ca-BWT calibration for *Globobulimina* spp. [*Weldeab et al.*, 2016].

It stands out that the H1 episode was marked by strong bottom water warming with an average value of 3.9 ± 0.5°C above that of the pre-H1 episode (Figures 4d and 6d). The onset of the warming is synchronous with the timing of changes in Ba/Ca and $\delta^{13}C$ records. The termination of bottom water warming occurred at 14 ± 0.2 kyr B.P., approximately 500 ± 200 years after the onset of AMOC intensification, as inferred from $^{231}Pa/^{230}Th$ records [*Bradtmiller et al.*, 2014; *McManus et al.*, 2004] and Bølling-Allerød warming in northern high latitude [*NGRIP-members*, 2004]. The BWT decline during the Bølling-Allerød was followed by bottom water warming of 5.2 ± 1.2°C whose timing and duration coincides with that of the YD. In contrast to the H1 record, the temperature rise during YD is not accompanied by an increase of refractory nutrients and

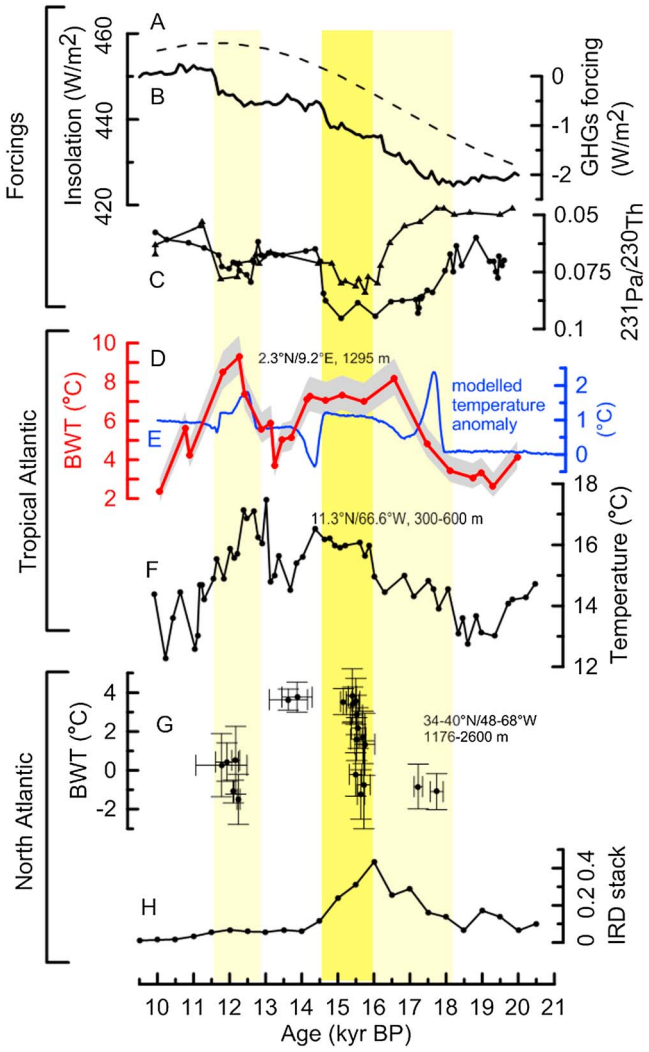

Figure 6. Climate forcings and comparison of the timing and magnitude of thermocline and middepth temperature between the tropical and North Atlantic middepths. (a) Solar insolation over 10°N in 21 July [*Laskar et al*., 2004], (b) changes in greenhouse gas forcings relative to the pre-industrial value [*Marcott et al*., 2014], and (c) estimates of relative AMOC changes: lines with triangle and circles indicate $^{231}Pa/^{230}Th$ records from the Iberian Margin [*Gherardi et al*., 2005] and dotted line the Bermuda rise [*McManus et al*., 2004], respectively. (d) Mg/Ca-based bottom water temperature (BWT) estimate with the gray envelop indicating uncertainty in the BWT estimate (this study), (e) model-based estimate of temperature at depth of 1295 (this study), (f) thermocline temperature estimates in the western tropical Atlantic [*Schmidt et al*., 2012], (g) clumped-isotope based BWT estimates across water depth between 1176 m and 2600 m in the western North Atlantic [*Thiagarajan et al*., 2014], and (h) a stack of 15 North Atlantic IRD records, arbitrary unit [*Stern and Lisiecki*, 2013]. Light yellow shading indicates the YD time interval and the early phase of H1. Dark yellow shading indicates H1 episode that coincide with peak values of $^{231}Pa/^{230}Th$ (strong AMOC weakening) (Figure 6c) and abrupt and large middepth warming in western North Atlantic (Figure 6f).

bottom water residence time (Figures 4–6). In summary, the MD03-2707 record reveals that the EEA middepth experienced a large-scale warming and changes in source or residence time of intermediate level water during the H1. The YD episode differs from H1 by showing the most prominent middepth warming and the absence of an enrichment of refractory nutrient, suggesting a relatively reduced impact of a weak freshwater forcing on the middepth of the eastern equatorial Atlantic.

3.2. Results of Transient Model Simulation

To explore the driving mechanisms of the bottom water warming and changes in EEA bottom water tracers, we carried out an idealized transient model simulation forced with freshwater input into the North Atlantic (Figure 3). In response to the freshwater forcing, the AMOC weakens significantly during H1 and YD (Figures 3b and 5b). In qualitative agreement with the proxy data (Figure 5d), the simulation results (Figure 5c) suggest a decrease of $\Delta^{14}C_{bottom\ water}$, an increase of bottom water nutrient concentration (Figure 5f), bottom water warming (Figure 6e), and a relative increase of Southern Ocean influence (Figure 5i). While freshwater forcing during YD results in a moderate weakening of the AMOC (Figure 5b), consistent with the proxy records, the simulation results do not show an increase of refractory nutrients (Figure 5f) and only a small increase of Southern Ocean-sourced water (Figure 5i).

According to the results of the model simulation, the enhanced bottom water residence time and increased refractory nutrients over our core site during H1 are a result of an increase of Southern Ocean-sourced water relative to the decreasing volume of North Atlantic Deep Water (Figures 3d and 5i). The reduction of the cold North Atlantic water inflow and the overall sluggish circulation during H1 enhances the influence of SST on the middepth temperature via downward diffusive heat exchanges, leading to significant intermediate water warming (Figure 6). Even though model and proxy results are in good qualitative agreement with respect to a bottom water temperature increase in response to an AMOC weakening, the simulated timing and amplitude of the warming differs from the Mg/Ca record.

One possible reason for this discrepancy is the abruptness of the simulated AMOC change (Figure 5b) vis-à-vis the slower reconstructed AMOC reorganization (Figure 5a).

Qualitatively consistent with the proxy record, the modeling results for YD indicate a BWT rise (Figure 6e) and a lack of nutrient enrichment (Figure 5). The difference in the strength and duration of the freshwater forcing during H1 and YD explains the deviant tracer imprints in the intermediate water depth of the equatorial Atlantic. The stronger bottom water warming during the YD relative to that of H1 can be partly explained by the elevated greenhouse gas and solar insolation forcings and their impact on the EEA SST (Figures 6a–6d). Taken together, the results of the model simulation qualitatively reproduce the prominent features found in the EEA deglacial proxy records. Both the model and proxy data indicate that the intermediate water of the eastern equatorial Atlantic responded sensitively to meltwater-induced AMOC weakening. Deviating from the proxy BWT reconstruction, the result of the model run does not show persistent bottom water warming after the termination of H1. Because the major BWT drop occurred 500 ± 200 years after the reinvigoration of the AMOC (Figure 6e), it is likely that the sustained warming in the tropical Atlantic middepth reflects an equatorward transport of relatively warm middepth North Atlantic water (see below).

3.3. Timing and Spatial Extent of Middepth Warming

A quantitative reconstruction of subsurface and middepth temperature changes in the tropical Atlantic during the last deglacial was so far limited to the western part of the basin [*Came et al*., 2007; *Schmidt et al*., 2012]. The middepth and thermocline warming of western tropical Atlantic during H1 and YD is estimated ~3°C and 2–4°C, respectively [*Came et al*., 2007; *Lynch-Stieglitz et al*., 2014; *Rühlemann et al*., 2004; *Schmidt et al*., 2012]. Taking uncertainties of the age models and temperature estimates into account, the magnitude and timing of western Atlantic middepth warming is comparable to and synchronous with these of the eastern equatorial Atlantic (Figures 6d and 6f). While age model uncertainties put constraints on the confidence of centennial-scale comparison, the persistent EEA middepth warming 500 ± 200 years after the end of H1 (Figures 4c and 6d) is also evident in the subsurface temperature record of the western tropical Atlantic [*Schmidt et al*., 2012]. Overall, thermocline and middepth warming in the western and eastern tropical Atlantic indicate a basin-wide and, therefore, large heat accumulation in response to an AMOC perturbation during H1 and YD, consistent an Atlantic thermocline deepening [*Cessi et al*., 2004; *Timmermann et al*., 2005].

Available BWT records from the North Atlantic middepth reveal a varying timing and pace of BWT rise during H1 (Figures 6) [*Marcott et al*., 2011; *Thiagarajan et al*., 2014]. Though the low resolution, a potential effect of carbonate ion concentration on the Mg/Ca and the multispecies nature of the Mg/Ca record do not allow a robust comparison of the pace and magnitude of thermal changes across the transition of last glacial and H1 episodes, a BWT reconstruction from the northwestern Atlantic middepth suggests H1 warming [*Marcott et al*., 2011]. While discontinuous, another record of western North Atlantic temperature estimates across the water depth between 1176 and 2600 m indicates an abrupt temperature rise of 6°C between 15.1 and 15.8 kyr B.P. [*Thiagarajan et al*., 2014] that coincides with the timing of the height of the AMOC decline, as inferred from $^{231}Pa/^{230}Th$ records [*Bradtmiller et al*., 2014] and the peak of ice-rafted debris (IRD) across the north Atlantic (Figure 6) [*Gherardi et al*., 2005; *McManus et al*., 2004; *Stern and Lisiecki*, 2013]. The gradual middepth warming in the tropical Atlantic (Figures 6d and 6f) preceded the abrupt warming of the North Atlantic middepth by about 3000 years (Figures 6b and 6c). Because of its spatial coverage and the robustness of its age model, we compare the temperature record from the North Atlantic middepth [*Thiagarajan et al*., 2014] with the thermocline and middepth temperature records from tropical Atlantic (Figures 6d–6g). While the discontinuity of the North Atlantic middepth record does not allow a detailed comparison of temperature trends throughout the H1 episode, the relatively abrupt and large (~6°C) warming at 15.1–15.8 kyr B.P. is unmatched by a comparable magnitude and pace of warming in the tropical Atlantic records that reveal a gradual BWT rise starting from 19 kyr B.P. (Figure 6). Conversely, the large tropical Atlantic middepth warming during the YD episode contrasts strongly with the concomitant cooling (relative to the Bølling-Allerøds) of North Atlantic middepth (Figure 6). These findings indicate a thermal decoupling between the tropical and North Atlantic middepths and challenge the notion of rapid heat exchanges between the middepths of the tropical and North Atlantic during H1 and YD [*Dokken et al*., 2013; *Petersen et al*., 2013; *Shaffer*, 2004]. We hypothesize that heat exchange was weak and the abrupt and

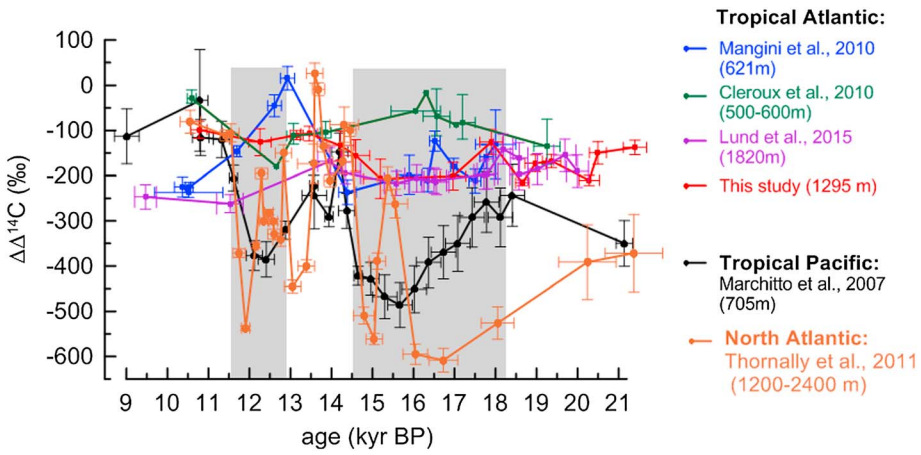

Figure 7. $\Delta\Delta^{14}C$ ($\Delta^{14}C$ benthic foraminifera/cold water coral minus $\Delta^{14}C$ atmosphere) reconstructed in tropical Atlantic [*Cléroux et al.*, 2011; *Freeman et al.*, 2015; *Lund et al.*, 2015; *Mangini et al.*, 2010], North Atlantic [*Thornalley et al.*, 2011], and tropical Pacific [*Marchitto et al.*, 2007b] cores.

delayed North Atlantic middepth warming most likely occurred in response to an outflow of warm Arctic and Nordic Sea subsurface water that has been recently identified [*Cronin et al.*, 2012; *Thornalley et al.*, 2015].

3.4. Young-to-Moderate Age of Middepth Atlantic Water During H1

The abrupt H1 warming in the middepth of North Atlantic [*Thiagarajan et al.*, 2014] was accompanied by the presence of very old water that has been initially interpreted to originate from the Southern Ocean [*Robertson et al.*, 2005; *Thiagarajan et al.*, 2014; *Thornalley et al.*, 2011]. Linking the very old middepth North Atlantic water to advection of Southern Ocean-sourced middepth water is at odds with our results from the middepth of tropical Atlantic that serves as a conduit for the AAIW. The upper part of northern tropical Atlantic middepth (≤1000 m water depth) appears to be marked by a strong influence of relatively young North Atlantic water [*Came et al.*, 2008; *Huang et al.*, 2014; *Xie et al.*, 2012, 2014]. Consistent with previous studies [*Chen et al.*, 2015; *Cléroux et al.*, 2011; *Freeman et al.*, 2015; *Lund et al.*, 2015; *Mangini et al.*, 2010; *Sortor and Lund*, 2011] our results reveal the absence of a radiocarbon-depleted middepth water in the tropical Atlantic during H1 (Figure 7). The implication of this observation is twofold. First, given the relatively young-to-moderate age of middepth water in the tropical Atlantic (Figure 7), it is difficult to reconcile that the strong radiocarbon depletion of middepth North Atlantic water can be solely attributed to entrainment of extremely old Southern Ocean water into the AAIW. An alternative explanation, as suggested in recent studies [*Thornalley et al.*, 2015; *Wilson et al.*, 2014], is that an overflow of radiocarbon-depleted Nordic Sea subsurface waters substantially contributed to the radiocarbon depletion of middepth North Atlantic water. The existence of strongly radiocarbon-depleted water in the middepth of the eastern tropical Pacific and Indian Ocean during H1 and YD has been interpreted to reflect a northward spread of upwelled, extremely old glacial water from the Pacific and Indian Ocean segments of the deep Southern Ocean [*Bryan et al.*, 2010; *Marchitto et al.*, 2007b]. In analogy to the interpretation of the tropical Pacific data [*Marchitto et al.*, 2007b], *Mangini et al.* [2010] suggested an invasion of radiocarbon-depleted Southern Ocean-sourced water into the tropical Atlantic middepth. In agreement with the growing lines of evidence from the tropical Atlantic [*Chen et al.*, 2015; *Cléroux et al.*, 2011; *Lund et al.*, 2015; *Sortor and Lund*, 2011], our $\Delta\Delta^{14}C$ record does not support the hypothesized spread of an extremely old middepth water from the Southern Ocean into the middepth of the tropical Atlantic [*Mangini et al.*, 2010]. One scenario is that large-scale upwellings of extremely old middepth water from the Southern Ocean during H1 and YD did not occur. Alternatively, if a northward spread of radiocarbon-depleted water occurred then air-sea exchanges of CO_2 and advective and diffusive mixing must had significantly diluted the radiocarbon-depleted water as it entrained into the AAIW and advected into the tropical Atlantic. Another scenario arises from proxy data that have been interpreted to suggest that during the early deglacial the deep South Atlantic was isolated from the middepth South Atlantic and that the latter shows no sign of ventilation events until 15 kyr B.P. [*Lund et al.*, 2015; *Rickaby et al.*, 2010; *Yu et al.*, 2014]. Depending which of the two scenarios is more likely, it has implication for our understanding of the mechanism that led to the early deglacial atmospheric CO_2 rise.

4. Summary and Conclusion

This study demonstrates that during H1 and YD the middepth of EEA was marked by a strong warming, with an average temperature rise of 3.9 ± 0.5°C and 5.2 ± 1.2°C, respectively. Together with the records from the western tropical Atlantic, the EEA record reveals a basin-wide and large-scale heat accumulation across the thermocline and middepth at times of a weakened AMOC. Our idealized transient model simulation qualitatively reproduces the major features of oceanographic changes and relates the middepth warming to a relative increase of downward heat diffusion due to the sluggish replenishment of cold middepth North Atlantic [*Cessi et al*., 2004]. The results of our thermal and water mass reconstructions during H1 and YD have an implication for our understanding of interhemispheric heat and water mass exchanges. A northward transport of extremely old Southern Ocean-sourced middepth water, as hypothesized in previous studies, is not consistent with the relatively young age of middepth water across the tropical Atlantic. Therefore, the hypothesized spread of old upwelled Southern Ocean-sourced water into the tropical Atlantic middepth may have not occurred or was rejuvenated by air-sea gas exchanges and advective/diffusive mixing as it was entrained into the AAIW and transported northward Atlantic. Contrasting the timing and pace of middepth warming during H1 and YD, a heat exchange between the tropical and North Atlantic middepth is not supported by the currently available data. Consequently, the rapid heat buildup in the middepth of North Atlantic must be related to changes within the subsurface and middepth of the northern high latitude.

Acknowledgments
We thank Georges Paradis for ICP-MS operation. This study was supported by UCSB start-up (S.W.), Hellmann Family Faculty Fund (S.W.), and NSF grants 1260696 (S.W.), 1400914 (A.T.), and 1341311 (A.T.). We thank the two anonymous reviewers and the Editor (Heiko Pälike) for their constructive comments on an earlier version of this paper. Data will be available at the NOAA Paleoclimatology (https://www.ncdc.noaa.gov/data-access/paleoclimatology-data) and personal website of the first author (http://www.geol.ucsb.edu/people/syee-weldeab).

References

Adkins, J. F., and E. A. Boyle (1997), Changing atmospheric $\Delta^{14}C$ and the record of deep water paleoventilation ages, *Paleoceanography*, *12*, 337–344, doi:10.1029/97PA00379.

Alvarez-Solas, J., A. Robinson, M. Montoya, and C. Ritz (2013), Iceberg discharges of the last glacial period driven by oceanic circulation changes, *Proc. Natl. Acad. Sci. U.S.A.*, *110*(41), 16,350–16,354, doi:10.1073/pnas.1306622110.

Barker, S., J. Chen, X. Gong, L. Jonkers, G. Knorr, and D. Thornalley (2015), Icebergs not the trigger for North Atlantic cold events, *Nature*, *520*(7547), 333–336, doi:10.1038/nature14330.

Berger, A. (1978), Long-term variations of caloric insolation resulting from the Earth's orbital elements, *Quat. Res.*, *9*, 139–167.

Blaauw, M., and J. A. Christen (2011), Flexible paleoclimate age-depth models using an autoregressive gamma process, *Bayesian Anal.*, *6*, 457–474, doi:10.1214/11-ba618.

Bradtmiller, L. I., J. F. McManus, and L. F. Robinson (2014), $^{231}Pa/^{230}Th$ evidence for a weakened but persistent Atlantic meridional overturning circulation during Heinrich Stadial 1, *Nat. Commun.*, *5*, doi:10.1038/ncomms6817.

Bryan, S. P., T. M. Marchitto, and S. J. Lehman (2010), The release of ^{14}C-depleted carbon from the deep ocean during the last deglaciation: Evidence from the Arabian Sea, *Earth Planet. Sci. Lett.*, *298*(1-2), 244–254, doi:10.1016/j.epsl.2010.08.025.

Came, R. E., W. B. Curry, D. W. Oppo, A. J. Broccoli, R. J. Stouffer, and J. Lynch-Stieglitz (2007), North Atlantic intermediate depth variability during the Younger Dryas: Evidence from benthic foraminiferal Mg/Ca and the Gfdl R30 coupled climate model, in *Ocean Circulation: Mechanisms and Impacts—Past and Future Changes of Meridional Overturning*, edited by A. Schmittner, J. C. H. Chiang, and S. R. Hemming, pp. 247–263, AGU, Washington, D. C., doi:10.1029/173GM16.

Came, R. E., D. W. Oppo, W. B. Curry, and J. Lynch-Stieglitz (2008), Deglacial variability in the surface return flow of the Atlantic meridional overturning circulation, *Paleoceanography*, *23*, PA1217, doi:10.1029/2007PA001450.

Cessi, P., K. Bryan, and R. Zhang (2004), Global seiching of thermocline waters between the Atlantic and the Indian-Pacific Ocean Basins, *Geophys. Res. Lett.*, *31*, L04302, doi:10.01029/02003GL019091.

Chen, T., L. F. Robinson, A. Burke, S. Southon, P. Spooner, P. J. Morris, and H. C. Ng (2015), Synchronous centennial abrupt events in the ocean and atmosphere during the last deglaciation, *Science*, *349*, 1537–1541.

Cléroux, C., P. deMenocal, and T. Guilderson (2011), Deglacial radiocarbon history of tropical Atlantic thermocline waters: Absence of CO_2 reservoir purging signal, *Quat. Sci. Rev.*, *30*(15-16), 1875–1882, doi:10.1016/j.quascirev.2011.04.015.

Cronin, T. M., G. S. Dwyer, J. Farmer, H. A. Bauch, R. F. Spielhagen, M. Jakobsson, J. Nilsson, W. M. Briggs, and A. Stepanova (2012), Deep Arctic Ocean warming during the last glacial cycle, *Nat. Geosci.*, *5*(9), 631–634, doi:10.1038/ngeo1557.

Decloedt, T., and D. S. Luther (2010), On a simple empirical parameterization of topography-catalyzed diapycnal mixing in the abyssal ocean, *J. Phys. Oceanogr.*, *40*(3), 487–508, doi:10.1175/2009JPO4275.1.

Dokken, T. M., K. H. Nisancioglu, C. Li, D. S. Battisti, and C. Kissel (2013), Dansgaard-Oeschger cycles: Interactions between ocean and sea ice intrinsic to the Nordic seas, *Paleoceanography*, *28*, 491–502, doi:10.1002/palo.20042.

Elderfield, H., J. Yu, P. Anand, T. Kiefer, and B. Nyland (2006), Calibrations for benthic foraminiferal Mg/Ca paleothermometry and the carbonate ion hypothesis, *Earth Planet. Sci. Lett.*, *250*(3-4), 633–649, doi:10.1016/j.epsl.2006.07.041.

Fichefet, T., and M. Maqueda (1997), Sensitivity of a global sea ice model to the treatment of ice thermodynamics and dynamics, *J. Geophys. Res.*, *102*(C6), 12,609–12,646, doi:10.1029/97JC00480.

Fichefet, T., S. Hovine, and J.-C. Duplessy (1994), A model study of the Atlantic thermohaline circulation during the last glacial maximum, *Nature*, *372*, 252–255.

Freeman, E., L. C. Skinner, A. Tisserand, T. Dokken, A. Timmermann, L. Menviel, and T. Friedrich (2015), An Atlantic–Pacific ventilation seesaw across the last deglaciation, *Earth Planet. Sci. Lett.*, *424*, 237–244, doi:10.1016/j.epsl.2015.05.032.

Friedrich, T., A. Timmermann, L. Menviel, O. Elison Timm, A. Mouchet, and D. M. Roche (2010), The mechanism behind internally generated centennial-to-millennial scale climate variability in an Earth system model of intermediate complexity, *Geosci. Model Dev.*, *3*(2), 377–389, doi:10.5194/gmd-3-377-2010.

Friedrich, T., A. Timmermann, T. Decloedt, D. S. Luther, and A. Mouchet (2011), The effect of topography-enhanced diapycnal mixing on ocean and atmospheric circulation and marine biogeochemistry, *Ocean Modell.*, *39*(3–4), 262–274, doi:10.1016/j.ocemod.2011.04.012.

Ganopolski, A., and R. Calov (2011), The role of orbital forcing, carbon dioxide and regolith in 100 kyr glacial cycles, *Clim. Past*, *7*(4), 1415–1425, doi:10.5194/cp-7-1415-2011.
Gebbie, G. (2014), How much did glacial North Atlantic water shoal?, *Paleoceanography*, *29*, 190–209, doi:10.1002/2013PA002557.
Gherardi, J., L. Labeyrie, J. McManus, R. Francois, L. Skinner, and E. Cortijo (2005), Evidence from the Northeastern Atlantic basin for variability in the rate of the meridional overturning circulation through the last deglaciation, *Earth Planet. Sci. Lett.*, *240*(3-4), 710–723, doi:10.1016/j.epsl.2005.09.061.
Goosse, H., E. Deleersnijder, T. Fichefet, and M. H. England (1999), Sensitivity of a global coupled ocean-sea ice model to the parameterization of vertical mixing, *J. Geophys. Res.*, *104*(C6), 13,681–13,695, doi:10.1029/1999JC900099.
Goosse, H., et al. (2010), Description of the Earth system model of intermediate complexity LOVECLIM version 1.2, *Geosci. Model Dev.*, *3*(2), 603–633, doi:10.5194/gmd-3-603-2010.
Hall, J. M., and L. H. Chan (2004), Ba/Ca in benthic foraminifera: Thermocline and middepth circulation in the North Atlantic during the last glaciation, *Paleoceanography*, *19*, PA4018, doi:10.1029/2004PA001028.
Hemming, S. R. (2004), Heinrich events: Massive late Pleistocene detritus layers of the North Atlantic and their global climate imprint, *Rev. Geophys.*, *42*, RG1005, doi:10.1029/2003RG000128.
Huang, K.-F., D. W. Oppo, and W. B. Curry (2014), Decreased influence of Antarctic intermediate water in the tropical Atlantic during North Atlantic cold events, *Earth Planet. Sci. Lett.*, *389*, 200–208, doi:10.1016/j.epsl.2013.12.037.
Key, R. M., A. Kozyr, C. L. Sabine, K. Lee, R. Wanninkhof, J. L. Bullister, R. A. Feely, F. J. Millero, C. Mordy, and T. H. Peng (2004), A global ocean carbon climatology: Results from Global Data Analysis Project (GLODAP), *Global Biogeochem. Cycles*, *18*, GB4031, doi:10.1029/2004GB002247.
Laskar, J., P. Robutel, F. Joutel, M. Gastineau, A. C. M. Correia, and B. Levrard (2004), A long-term numerical solution for the insolation quantities of the Earth, *Astron. Astrophys.*, *428*, 261–285.
Lea, D., and E. Boyle (1989), Barium content of benthic foraminifera controlled by bottom water composition, *Nature*, *338*, 751–753.
Liu, Z., et al. (2009), Transient simulation of last deglaciation with a new mechanism for Bolling-Allerod warming, *Science*, *325*(5938), 310–314, doi:10.1126/science.1171041.
Lund, D. C., A. C. Tessin, J. L. Hoffman, and A. Schmittner (2015), Southwest Atlantic water mass evolution during the last deglaciation, *Paleoceanography*, *30*, 477–494, doi:10.1002/2014PA002657.
Luthi, D., et al. (2008), High-resolution carbon dioxide concentration record 650,000-800,000 years before present, *Nature*, *453*(7193), 379–382, doi:10.1038/nature06949.
Lynch-Stieglitz, J., M. W. Schmidt, L. Gene Henry, W. B. Curry, L. C. Skinner, S. Mulitza, R. Zhang, and P. Chang (2014), Muted change in Atlantic overturning circulation over some glacial-aged Heinrich events, *Nat. Geosci.*, *7*(2), 144–150, doi:10.1038/ngeo2045.
Mangini, A., J. M. Godoy, M. L. Godoy, R. Kowsmann, G. M. Santos, M. Ruckelshausen, A. Schroeder-Ritzrau, and L. Wacker (2010), Deep sea corals off Brazil verify a poorly ventilated Southern Pacific Ocean during H2, H1 and the Younger Dryas, *Earth Planet. Sci. Lett.*, *293*(3–4), 269–276, doi:10.1016/j.epsl.2010.02.041.
Marchitto, T. M., S. P. Bryan W. B. Curry, and D. C. McCorkle (2007a), Mg/Ca temperature calibration for the benthic foraminifer *Cibicidoides pachyderma*, *Paleoceanography*, *22*, PA1203, doi:10.1029/2006PA001287.
Marchitto, T. M., S. J. Lehman, J. D. Ortiz, J. Flueckiger, and A. van Geen (2007b), Marine radiocarbon evidence for the mechanism of deglacial atmospheric CO_2 rise, *Science*, *316*(5830), 1456–1459.
Marcott, S. A., et al. (2011), Ice-shelf collapse from subsurface warming as a trigger for Heinrich events, *Proc. Natl. Acad. Sci. U.S.A.*, *108*(33), 13,415–13,419, doi:10.1073/pnas.1104772108.
Marcott, S. A., et al. (2014), Centennial-scale changes in the global carbon cycle during the last deglaciation, *Nature*, *514*(7524), 616–619, doi:10.1038/nature13799.
Martin, P. A., and D. W. Lea (2002), A simple evaluation of cleaning procedures on fossil benthic foraminiferal Mg/Ca, *Geochem. Geophys. Geosyst.*, *3*(10), 8401, doi:10.1029/2001GC000280.
McManus, J. F., R. Francois, J.-M. Gherardi, L. D. Keigwin, and S. Brown-Leger (2004), Collapse and rapid resumption of Atlantic meridional circulation linked to deglacial climate changes, *Nature*, *428*, 834–837.
Menviel, L., A. Timmermann, O. E. Timm, and A. Mouchet (2011), Deconstructing the Last Glacial termination: The role of millennial and orbital-scale forcings, *Quat. Sci. Rev.*, *30*(9-10), 1155–1172, doi:10.1016/j.quascirev.2011.02.005.
Menviel, L., F. Joos, and S. P. Ritz (2012), Simulating atmospheric CO_2, ^{13}C and the marine carbon cycle during the Last Glacial–Interglacial cycle: Possible role for a deepening of the mean remineralization depth and an increase in the oceanic nutrient inventory, *Quat. Sci. Rev.*, *56*, 46–68, doi:10.1016/j.quascirev.2012.09.012.
Mouchet, A. (2011), A 3D model of ocean biogeochemical cycles and ocean ventilation studies, Dissertation, 1–87 pp.
NGRIP-members (2004), High-resolution record of Northern Hemisphere climate extending into the last interglacial period, *Nature*, *431*, 147–151.
Oppo, D. W., W. B. Curry, and J. F. McManus (2015), What do benthic δ13C and δ18O data tell us about Atlantic circulation during Heinrich Stadial 1?, *Paleoceanography*, *30*, 353–368, doi:10.1002/2014PA002667.
Opsteegh, J., R. Haarsma, F. Selten, and A. Kattenberg (1998), ECBILT: A dynamic alternative to mixed boundary conditions in ocean models, *Tellus A*, *50*, 348–367.
Peeters, F., C. J. Brummer, and G. Ganssen (2002), The effect of upwelling on the distribution and stable isotope composition of Globigerina bulloides and Globigerinoides ruber (planktic foraminifera) in modern surface waters of the NW Arabian Sea, *Global Planet. Change*, *34*, 269–291.
Petersen, S. V., D. P. Schrag, and P. U. Clark (2013), A new mechanism for Dansgaard-Oeschger cycles, *Paleoceanography*, *28*, 24–30, doi:10.1029/2012PA002364.
Reimer, P. J., et al. (2013), IntCal13 and Marine13 radiocarbon age calibration curves 0–50,000 years cal BP, *Radiocarbon*, *55*, 1869–1887.
Renssen, H., A. Mairesse, H. Goosse, P. Mathiot, O. Heiri, D. M. Roche, K. H. Nisancioglu, and P. J. Valdes (2015), Multiple causes of the Younger Dryas cold period, *Nat. Geosci.*, *8*(12), 946–949, doi:10.1038/ngeo2557.
Rickaby, R. E. M., H. Elderfield, N. Roberts, C. D. Hillenbrand, and A. Mackensen (2010), Evidence for elevated alkalinity in the glacial Southern Ocean, *Paleoceanography*, *25*, PA1209, doi:10.1029/2009PA001762.
Robbins, L. L., M. E. Hansen, J. A. Kleypas, and S. C. Meylan (2010), CO2calc—A user-friendly seawater carbon calculator for Windows, Max OS X, and iOS (iPhone), in *U.S. Geological Survey Open-File Report 2010–1280*, edited.
Robertson, L. F., J. F. Adkins, L. D. Keigwin, J. Southon, S. P. Fernandez, S.-L. Wanfg, and D. S. Scheirer (2005), Radiocarbon variability in the western North Atlantic during the last deglaciation, *Science*, *310*, 1469–1473.
Roche, D. M., T. M. Dokken, H. Goosse, H. Renssen, and S. L. Weber (2007), Climate of the Last Glacial Maximum: Sensitivity studies and model-data comparison with the LOVECLIM coupled model, *Clim. Past*, *3*(2), 205–224, doi:10.5194/cp-3-205-2007.

Rosenthal, Y., C. H. Lear, D. W. Oppo, and B. K. Linsley (2006), Temperature and carbonate ion effects on Mg/Ca and Sr/Ca ratios in benthic foraminifera: Aragonitic species Hoeglundina elegans, *Paleoceanography*, *21*, PA1007, doi:10.1029/2005PA001158.

Rühlemann, C., S. Mulitza, G. Lohmann, A. Paul, M. Prange, and G. Wefer (2004), Intermediate depth warming in the tropical Atlantic related to weakened thermohaline circulation: Combining paleoclimate data and modeling results for the last deglaciation, *Paleoceanography*, *19*, PA1025, doi:10.1029/2003PA000948.

Ryan, W. B. F., et al. (2009), Global multi-resolution topography synthesis, *Geochem. Geophys. Geosyst.*, *10*, Q03014, doi:10.1029/2008GC002332.

Schlitzer, R. (2000), Electronic atlas of WOCE hydrographic and tracer data now available, *Eos Trans. AGU*, *81*, 45.

Schmidt, M. W., P. Chang, J. E. Hertzberg, T. R. Them 2nd, L. Ji, and B. L. Otto-Bliesner (2012), Impact of abrupt deglacial climate change on tropical Atlantic subsurface temperatures, *Proc. Natl. Acad. Sci. U.S.A.*, *109*(36), 14,348–14,352, doi:10.1073/pnas.1207806109.

Schmitt, J., et al. (2012), Carbon isotope constraints on the deglacial CO_2 rise from ice cores, *Science*, *336*(6082), 711–714, doi:10.1126/science.1217161.

Schmittner, A., N. Gruber, A. C. Mix, R. M. Key, A. Tagliabue, and T. K. Westberry (2013), Biology and air-sea gas exchange controls on the distribution of carbon isotope ratios (δ13C) in the ocean, *Biogeosciences*, *10*(9), 5793–5816, doi:10.5194/bg-10-5793-2013.

Shaffer, G. (2004), Ocean subsurface warming as a mechanism for coupling Dansgaard-Oeschger climate cycles and ice-rafting events, *Geophys. Res. Lett.*, *31*, L24202, doi:10.1029/22004GL020968.

Shakun, J. D., P. U. Clark, F. He, S. A. Marcott, A. C. Mix, Z. Liu, B. Otto-Bliesner, A. Schmittner, and E. Bard (2012), Global warming preceded by increasing carbon dioxide concentrations during the last deglaciation, *Nature*, *484*(7392), 49–54, doi:10.1038/nature10915.

Skinner, L. C., and H. Elderfield (2007), Rapid fluctuations in the deep North Atlantic heat budget during the last glacial period, *Paleoceanography*, *22*, PA1205, doi:10.1029/2006PA001338.

Sortor, R. N., and D. C. Lund (2011), No evidence for a deglacial intermediate water $\Delta^{14}C$ anomaly in the SW Atlantic, *Earth Planet. Sci. Lett.*, *310*(1-2), 65–72, doi:10.1016/j.epsl.2011.07.017.

Stern, J. V., and L. E. Lisiecki (2013), North Atlantic circulation and reservoir age changes over the past 41,000 years, *Geophys. Res. Lett.*, *40*, 3693–3697, doi:10.1002/grl.50679.

Stocker, T. F., A. Timmermann, M. Renold, and O. Timm (2007), Effects of salt compensation on the climate model response in simulations of large changes of the Atlantic meridional overturning circulation, *J. Clim.*, *20*(24), 5912–5928, doi:10.1175/2007JCLI1662.1.

Thiagarajan, N., A. V. Subhas, J. R. Southon, J. M. Eiler, and J. F. Adkins (2014), Abrupt pre-Bolling-Allerod warming and circulation changes in the deep ocean, *Nature*, *511*(7507), 75–78, doi:10.1038/nature13472.

Thornalley, D. J. R., S. Barker, W. S. Broecker, H. Elderfield, and I. N. McCave (2011), The deglacial evolution of North Atlantic deep convection, *Science*, *331*(6014), 202–205, doi:10.1126/science.1196812.

Thornalley, D., H. Elderfield, and I. N. McCave (2010), Intermediate and deep water paleoceanography of the northern North Atlantic over the past 21,000 years, *Paleoceanography*, *25*, PA1211, doi:10.1029/2009PA001833.

Thornalley, D., H. A. Bauch, G. Gebbie, W. Guo, M. Ziegler, S. M. Bernasconi, S. Barker, L. C. Skinner, and J. Yu (2015), A warm and poorly ventilated deep Arctic Mediterranean during the last glacial period, *Science*, *349*(6249), 706–710, doi:10.1126/science.aaa9554.

Timmermann, A., U. Krebs, F. Justino, H. Goosse, and T. Ivanochko (2005), Mechanisms for millennial-scale global synchronization during the last glacial period, *Paleoceanography*, *20*, PA4008, doi:10.1029/2004PA001090.

Wanninkhof, R. (1992), Relationship between wind speed and gas exchange over the ocean, *J. Geophys. Res.*, *97*(C5), 7373–7382, doi:10.1029/92JC00188.

Weldeab, S., D. W. Lea, R. R. Schneider, and N. Andersen (2007), 155,000 years of West African monsoon and ocean thermal evolution, *Science*, *316*(5829), 1303–1307, doi:10.1126/science.1140461.

Weldeab, S., D. W. Lea, H. Oberhänsli, and R. R. Schneider (2014a), Links between southwestern tropical Indian Ocean SST and precipitation over southeastern Africa over the last 17kyr, *Palaeogeogr. Palaeoclimatol. Palaeoecol.*, *410*, 200–212, doi:10.1016/j.palaeo.2014.06.001.

Weldeab, S., V. Menke, and G. Schmiedl (2014b), The pace of East African monsoon evolution during the Holocene, *Geophys. Res. Lett.*, *41*, 1724–1731, doi:10.1002/2014GL059361.

Weldeab, S., A. Arce, and S. Kasten (2016), Mg/Ca-DCO3-temperature calibration for Globobulimina spp.: A sensitive paleothermometer for deep-sea temperature reconstruction, *Earth Planet. Sci. Lett.*, *438*, 95–102, doi:10.1016/j.epsl.2016.01.009.

Wilson, D. J., K. C. Crocket, T. van de Flierdt, R. L. Flierdt, and J. A. Adkins (2014), Dynamic intermediate ocean circulation in the North Atlantic during Heinrich Stadial 1: A radiocarbon and neodymium isotope perspective, *Paleoceanography*, *29*, 1072–1093, doi:10.1002/2014PA002674.

Xie, R. C., F. Marcantonio, and M. W. Schmidt (2012), Deglacial variability of Antarctic Intermediate Water penetration into the North Atlantic from authigenic neodymium isotope ratios, *Paleoceanography*, *27*, PA3221, doi:10.1029/2012PA002337.

Xie, R. C., F. Marcantonio, and M. W. Schmidt (2014), Reconstruction of intermediate water circulation in the tropical North Atlantic during the past 22,000 years, *Geochim. Cosmochim. Acta*, *140*, 455–467, doi:10.1016/j.gca.2014.05.041.

Yu, J., R. F. Anderson, Z. Jin, L. Menviel, F. Zhang, F. J. Ryerson, and E. J. Rohling (2014), Deep South Atlantic carbonate chemistry and increased interocean deep water exchange during last deglaciation, *Quat. Sci. Rev.*, *90*, 80–89, doi:10.1016/j.quascirev.2014.02.018.